Ground Interference Effects on Subsonic Dynamic Stall in Pitch and Plunge

L. E. Ericsson* and J. P. Reding†
Lockheed Missiles & Space Company, Inc., Sunnyvale, California

An earlier developed analytic method for predicting dynamic stall is extended to high subsonic speeds to include both pitching and plunging oscillations in the presence of ground plane interference. Theoretical relationships are derived for the interdependence of unsteady and steady aerodynamics, providing the means for analytic extrapolation of subscale dynamic experimental data to full-scale flow conditions.

Nomenclature

a = effective time lag parameter
c = two-dimensional chord length
f = frequency
h = maximum thickness
M = Mach number
m_p = sectional pitching moment, coefficient $c_m = m_p/(\rho V^2/2)c$
n = sectional normal force, coefficient $c_n = n/(\rho V^2/2)c$
p = static pressure, coefficient $C_p = (p-p_\infty)/(\rho V^2/2)$
q = pitch rate
t = time
V = crossflow velocity
$\bar{V}$ = convection velocity
x = horizontal chordwise coordinate
z = vertical coordinate
α = angle of attack
α_0 = trim or time-average angle of attack
β = phase lag, $=\omega\Delta t$
Δ = increment and amplitude
Δh = gap size, distance to ground plane
Δt = time lag
ζ = dimensionless z coordinate, $=z/c$
θ = perturbation in pitch or torsion
ξ = dimensionless x coordinate, $=x/c$
ρ = air density
τ = dimensionless time $=Vt/c$
ψ = phase angle, $=\omega t$
$\omega, \bar{\omega}$ = oscillation frequency, $\omega=2\pi f$, $=\bar{\omega}c/V$, respectively

Subscripts

a = attached flow
b = base
d = discontinuity
h = hysteresis
OC = oscillation center and moment reference axis
s = separated flow
$1,2$ = numbering subscripts for conditions on both sides of the aerodynamic discontinuity
∞ = freestream conditions

Superscripts

i = separation-induced, e.g., $\Delta^i c_n$ = separation-induced normal force

Derivative Symbols

$c_{m_\alpha} = \partial c_m/\partial\alpha$
$\dot{\alpha} = \partial\alpha/\partial t$
$c_{mq} = \partial c_m/\partial\left(\frac{cq}{V}\right)$
$c_{m\dot{\alpha}} = \partial c_m/\partial\left(\frac{c\dot{\alpha}}{V}\right)$
$c_{n_{\dot{z}}} = \partial c_n/\partial\left(\frac{\dot{z}}{V}\right)$
$c_{m_{\dot{\theta}}} = c_{mq} + c_{m\dot{\alpha}}$
$\bar{c}_{n\dot{z}} = c_{n\theta} + c_{n\dot{z}}$
$c_{\dot{m}\dot{\theta}}, c_{\dot{n}\dot{z}}$ = integrated mean value

Introduction

In an earlier publication[1] it was shown how the method developed for dynamic stall analysis at low speeds[2,3] could be extended to high subsonic speeds to include the dynamic effects of shock-boundary layer interaction. In the present paper the analysis of Ref. 1 is extended to include plunging motion in addition to the pitching oscillations considered in Ref. 1, and to consider ground interference effects through the transonic speed range, where the ground plane introduces an inlet-like flow phenomenon. The "airfoil" is the rectangular cross section of the Space Shuttle cable trays and the ground plane represents the surface of the external tank, above which the cable trays are mounted on brackets.[4]

Discussion

Figure 1 illustrates the flow phenomenon introduced by the ground plane at transonic speeds. At $M=0.7$ and $\alpha<0$ the flow on the underside of the Space Shuttle cable tray exhibits the same type of shock-induced flow separation characteristics[4,5] (Fig. 1a) as the leeside of a high performance airfoil, as was demonstrated in Ref. 1. However, at $M=0.9$ the flow becomes choked in the channel between the bottom of the cross section and the ground plane (Fig. 1b). The flow in the "inlet" accelerates to supersonic speeds. This local supersonic speed region is terminated by a strong shock, which generates a pressure rise and associated flow

Presented as Paper 83-0889 at the AIAA/ASME/ASCE/AHS Structures, Structural Dynamics and Materials Conference, Lake Tahoe, Nev., May 2-4, 1983; received Feb. 7, 1984; revision received Aug. 13, 1984. Copyright © American Institute of Aeronautics and Astronautics, Inc., 1984. All rights reserved.

*Senior Consulting Engineer. Fellow AIAA.
†Staff Engineer. Associate Fellow AIAA.

separation. At $\alpha=0$ and 1 deg the flow aft of the shock is reaccelerated to supersonic speeds, and this new supersonic flow region is terminated by another strong shock, which provides the pressure rise to the downstream pressure level (i.e., topside pressure). When the cable tray is pitched from $\alpha=1$ to 1.5 deg the two-shock configuration changes to a single strong shock at the channel entrance. The resulting extensive flow separation causes a completely subsonic flow behavior through the rest of the channel.

This sudden flow change generates a discontinuous increase of the pressures on the bottom side, resulting in a positive normal force discontinuity (Δc_n). The aerodynamic center of pressure is located aft of the pitching axis (Fig. 1b) and the corresponding moment discontinuity (Δc_m) is statically stabilizing (Fig. 2).

Oil flow photographs at $M=0.9$, taken during the dynamic test,[6] confirm the existence of the earlier discussed double and single shock systems at $\alpha=0$ and 2 deg (Fig. 3). The photographs also indicate that the forward shock is highly skewed, an "inlet-behavior" that will be discussed later in more detail. Figure 4a shows the unsteady characteristics for the cable tray in the presence of the ground plane. It can be seen that the main effect of a change of the model span‡ was to move the critical Mach number at which a change occurs from a pure ground interference effect to the inletlike flow behavior, described earlier in Figs. 1b-3. Figure 4b shows that for $\alpha=-1$ deg and 0 the pressure distribution data for $M=0.7$ assume a great likeness to those at $\alpha=1$ and 1.5 deg for $M=0.9$ (Fig. 1b), indicating the existence of dual shocks also at $M=0.7$ for -1 deg $<\alpha<0$. When the angle of attack is increased above $\alpha=0$ the second shock disappears and a single strong shock is formed, similar to what happened at $M=0.9$ when α was increased above $\alpha=1$ deg (Fig. 1b). At $M=0.7$, however, the resulting force change is centered around the midchord rotation center and causes no significant moment change (Fig. 2).

At $\alpha=0$ and $0.7<M<0.9$, perturbing α to $\alpha>0$ will restrict the channel exit area and move the rear shock forward. This generates a moment contribution that becomes less statically stabilizing as the rear, second shock moves upstream with decreasing Mach number. The dynamic effects are opposite due to time lag effects,[1] explaining the continually increasing damping when the Mach number is decreased from $M=0.9$ to $M=0.7$ (Fig. 4a).

The flow pictures in Fig. 3 show that the "inlet shock" is slanted away from the leading edge of the cable tray. As it has to become normal before reaching the ground plane, it is highly curved, concave in shape, as sketched in Fig. 4b. This provides the mechanism needed to respond to the exit area restriction resulting at increasing angle of attack, as is illustrated in Fig. 4c. The pressure data support the inlet behavior suggested by the flow sketches. When α is increased, the "inlet shock" has to become much steeper to reduce the velocity and thereby the mass flow in spite of the increase of the inlet capture area.§ This explains the extremely steep increase of the pressure level at the leading edge with increasing α, indicating a rapid decrease of the inlet velocity (for $\alpha>0$ at $M=0.7$ and $\alpha>1$ deg at $M=0.9$, Fig. 4c). The discontinuous aerodynamic characteristics occur in connection with the change from the two-shock to the single-shock channel flow configuration. Based on the results in Fig. 4c, one would expect the discontinuity to occur at -1 deg $<\alpha<1.5$ deg in the Mach number range $0.7\leq M\leq 0.9$.

At $M<0.7$, the 1.25 deg pitching amplitude used in the dynamic test[6] does not restrict the channel exit area enough at $\alpha=0$ to cause inlet choking, and the regular shock-induced effects discussed in Ref. 1 are realized with associated decrease in the damping level. Thus, the abrupt change of damping level at $M\approx 0.7$ (Fig. 4a) can be explained by the different types of ground plane interference existing for $M>0.7$ and $M<0.7$.

Analysis of Ground Plane Interference

At $M<0.7$ the ground plane provides the regular type of ground interference. Assuming the channel to be truly closed

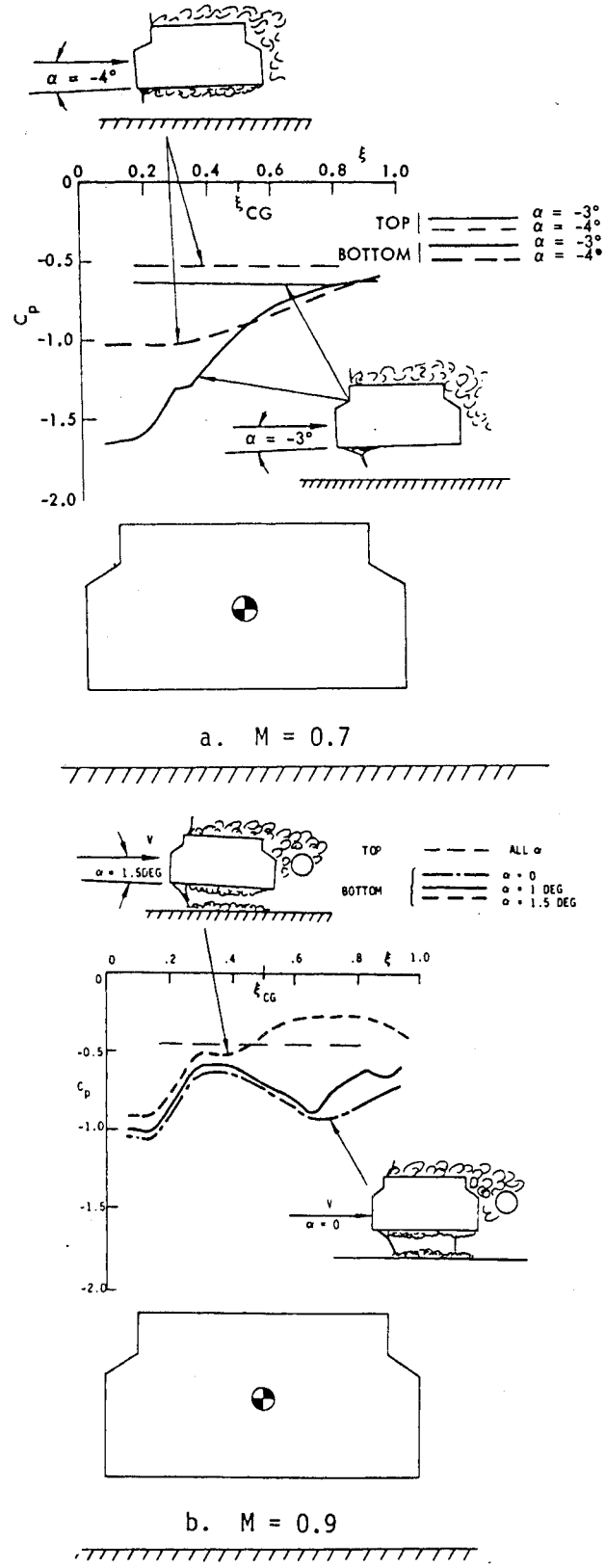

Fig. 1 Static pressure distribution on the Space Shuttle cable tray.[5]

‡For blockage reasons the span had to be decreased from 16 to 12 cm when adding the ground plane.[6]

§The cable tray pivots around midchord to change α.

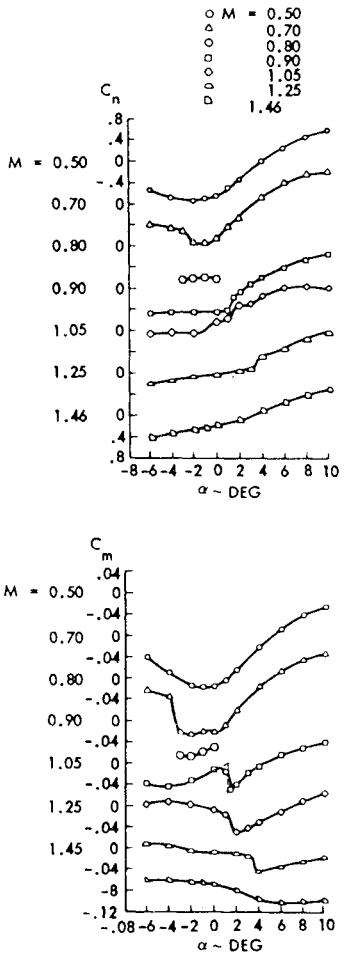

Fig. 2 Static aerodynamic characteristics of the Space Shuttle cable tray.[5]

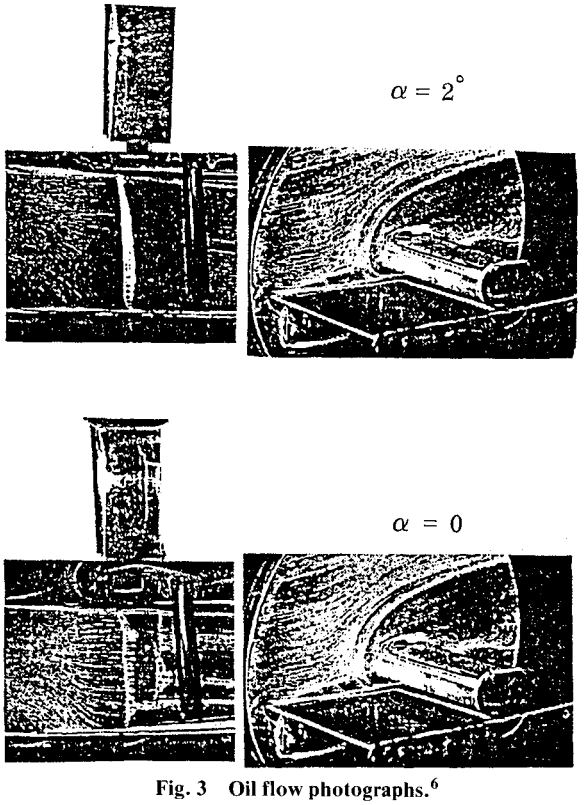

Fig. 3 Oil flow photographs.[6]

at the sides, as in the static test,[5] one obtains the following continuity and Bernoulli equations for incompressible flow:

$$\left[\frac{\Delta h}{c}-\left(\xi-\frac{1}{2}\right)\alpha\right]V=\text{const} \tag{1}$$

$$p+\frac{\rho_\infty V^2}{2}=\text{const} \tag{2}$$

Letting the streamtube height at upstream infinity be h_∞, Eq. (1) gives

$$\frac{V}{V_\infty}=\frac{h_\infty/c}{\Delta h/c-(\xi-1/2)\alpha} \tag{3}$$

Using freestream conditions as a reference, Eq. (2) becomes

$$C_p=1-\left(\frac{V}{V_\infty}\right)^2 \tag{4}$$

Combining Eqs. (3) and (4) gives

$$\frac{1-C_p}{1-C_{p_b}}=\left[\frac{(\Delta h/c)-(\alpha/2)}{(\Delta h/c)-(\xi-1/2)\alpha}\right]^2 \tag{5}$$

That is,

$$C_p=1-(1-C_{p_b})\left[\frac{(\Delta h/c)-(\alpha/2)}{(\Delta h/c)-(\xi-1/2)\alpha}\right]^2 \tag{6}$$

Differentiating Eq. (6) one obtains

$$C_{p_\alpha}=2(1-C_{p_b})\frac{(1-\xi)(\Delta h/c)}{[(\Delta h/c)-(\xi-1/2)\alpha]^2} \tag{7}$$

The incompressible channel flow contribution to c_{n_α} at $\alpha=0$ is[¶]

$$(c_{n_\alpha})_{CH}=\int_0^1 C_{p_\alpha}\mathrm{d}\xi=(1-C_{p_b})/(\Delta h/c) \tag{8}$$

In compressible flow, applying the Prandtl-Glauert correction gives

$$(c_{n_\alpha})_{CH}=(1-C_{pb})/(\Delta h/c)\sqrt{1-M^2};\ M\le 0.9 \tag{9}$$

The contribution to c_{m_α} is

$$(c_{m_\alpha})_{CH}=-\int_0^1 C_{p_\alpha}(\xi-\xi_{OC})\mathrm{d}\xi \tag{10}$$

$$=-(C_{n_\alpha})_{CH}(1/3-\xi_{OC})$$

According to Eq. (6) of Ref. 1 the corresponding contribution to the damping derivative is

$$(c_{m\dot\theta})_{CH}=-(\Delta\tau)_{CH}(c_{m\alpha})_{CH} \tag{11}$$

For the regular ground interference effect existing at $\alpha<0$ and $M<0.7$, the time lag $(\Delta\tau)_{CH}$ is the same as for the leeside flow on a regular airfoil.[1] At $M>0.7$, however, the inlet-like flow introduces time lag mechanisms not encountered in earlier dynamic stall analyses.[1-4] and the time lag has to be

[¶]This applies also with less than 10% error to $|\alpha|\le 3°$.

determined experimentally. As for the case of $M=0.7$, analyzed in Ref. 1, the aerodynamic characteristics become discontinuous for certain angles of attack and a nonlinear analysis is needed.

Nonlinear Analysis

Figure 4 shows that the jumpwise change of the aerodynamic characteristics associated with the discontinuous channel flow phenomenon (Fig. 2) would occur at $0<\alpha<1$ deg at $M=0.7$ and at 1 deg $<\alpha<1.5$ deg at $M=0.9$. Consequently, no oscillation with amplitude $\Delta\theta=1.25$ deg around $\alpha=0$ is possible in the Mach number range $0.7<M<0.9$ without "catching" the discontinuity. Thus, a nonlinear analysis is required for prediction of the damping (Fig. 4a). The needed detailed static experimental results[5] for such an analysis are only available for $M\approx 0.9$.

The highly nonlinear damping characteristics measured** at $M=0.92$ on the sharp-edged Space Shuttle cable tray are shown in Fig. 5. The data indicate that the sudden change of the shock-induced separated flow on the bottom side, which happens at 1 deg $<\alpha<1.5$ deg in the static test (Fig. 1b), occurs at $\alpha\leq 1$ deg in the dynamic test. The topside flow remains totally separated. Thus, the infinitesimal amplitude damping, $c_{m\dot{\theta}}$, is obtained from the bottom side.

When the channel flow between the bottom of the cross section and the ground plane becomes choked, as is the case for $M>0.7$ and $\alpha\geq 0$ (Fig. 4c), its aerodynamic characteristics are determined solely by the channel geometry, as has been verified by experimental results.[9]

As the insensitivity to frequency of the measured damping[6] (Fig. 5) shows that no static hysteresis is present, Eq. (14) from Ref. 1 can be applied.

$$c_{m_{\dot{\theta}_S}}=\frac{c_{m_{\dot{\theta}_1}}+c_{m_{\dot{\theta}_2}}}{2}+\frac{c_{m_{\dot{\theta}_1}}-c_{m_{\dot{\theta}_2}}}{\pi}\left[\arcsin\left(\frac{\alpha_d-\alpha_0}{\Delta\theta}\right)+\frac{\alpha_d-\alpha_0}{\Delta\theta}\times\sqrt{1-\left(\frac{\alpha_d-\alpha_0}{\Delta\theta}\right)^2}\right]-\frac{2a\Delta c_m}{\pi\alpha_d}\frac{\alpha_d}{\Delta\theta}\sqrt{1-\left(\frac{\alpha_d-\alpha_0}{\Delta\theta}\right)^2} \tag{12}$$

The discontinuity at $\alpha=-1.5$ deg for $M=0.9$ in Fig. 2 is $\Delta c_m=-0.08$. In the dynamic test the discontinuity occurred at $\alpha-1.0$ deg rather than at $\alpha=1.5$ deg. The time lag parameter $a=(\Delta\tau)_{CH}$ can be obtained by applying Eq. (11) to the experimental results[6] in Fig. 6. The difference between the results at $M=0.94$ with and without the web is caused by channel flow effects. One obtains $a=(\Delta\tau)_{CH}=2.8$. Still needed before Eq. (12) can be used are the values of the infinitesimal amplitude damping levels $c_{m_{\dot{\theta}_1}}$ and $c_{m_{\dot{\theta}_2}}$ on both sides of the discontinuity. The experimental results at $\alpha=-1$ deg and 3 deg should represent these levels, as the 1.25 deg amplitude oscillation at those angles of attack will not "catch" the discontinuity at $\alpha=1$ deg. Figure 5 gives $c_{m_{\dot{\theta}_1}}\approx -2.2$ and $c_{m_{\dot{\theta}_2}}\approx -3.9$. The static characteristics for $M=0.9$ in Fig. 2 indicate that c_{m_α} is constant on both sides of the discontinuity. As a matter of fact, the moment discontinuity, $\Delta c_m=-0.08$, is obtained by using the linear $C_m(\alpha)$ characteristics indicated by a dashed line in Fig. 2. Thus, the measured damping values, $c_{m\dot{\theta}_1}\approx -2.2$ and $c_{m\dot{\theta}_2}\approx -3.9$, should represent the infinitesimal amplitude damping levels on both sides of the aerodynamic discontinuity.

With these values, Eq. (12) gives the results shown in Fig. 7. The agreement between prediction and experiment is good, particularly for the maximum adverse damping at $\alpha=\alpha_d=1$ deg (Fig. 8). It is true that for the inletlike flow existing at $M=0.92$, the nonlinear damping characteristics caused by the aerodynamic discontinuity at $\alpha\approx 1$ deg could not be computed using only static experimental data, as was done for $M=0.7$ at

**Note that the dynamic derivatives in Ref. 6 are referenced to $cq/2V$ and $c\dot{\alpha}/2V$ rather than to cq/V and $c\dot{\alpha}/V$, as used herein.

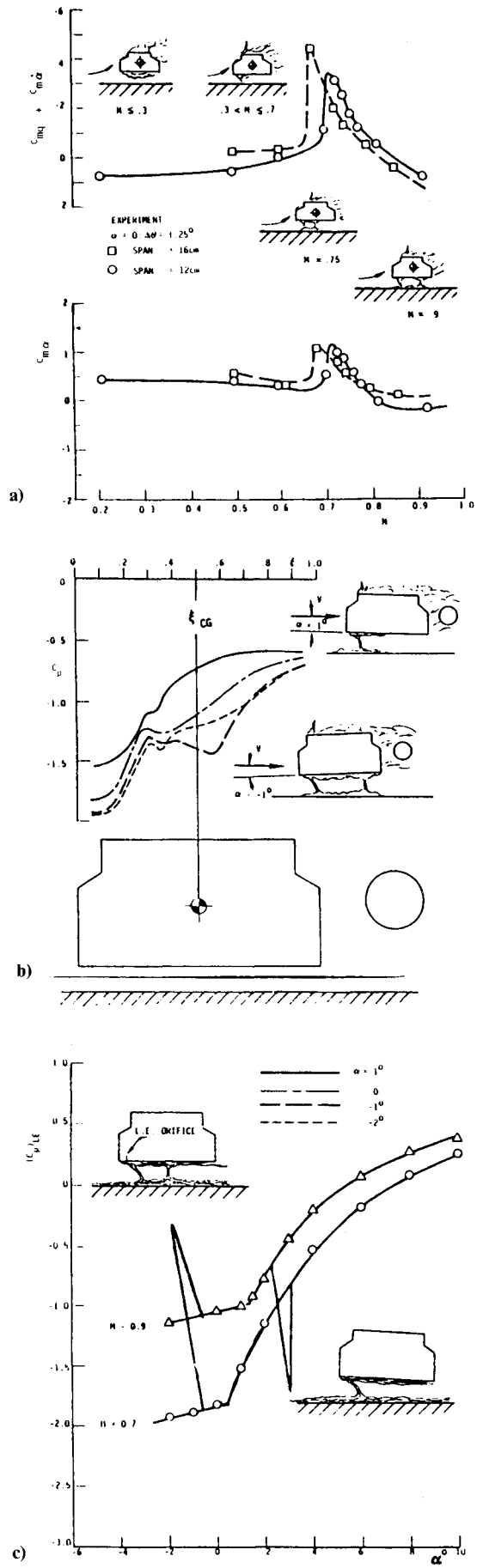

Fig. 4 Steady and unsteady aerodynamic characteristics of the Space Shuttle cable tray. a) dynamic characteristics at $\alpha=0$; b) static pressure distribution at $M=0.7$; c) leading edge pressure at $M=0.7$ and $M=0.9$.

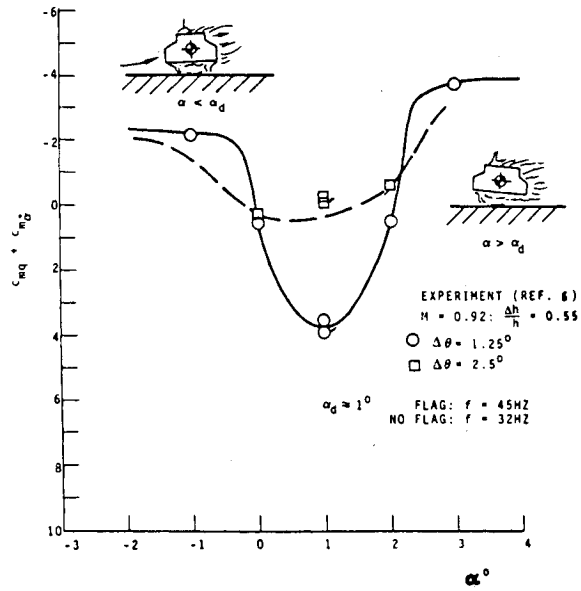

Fig. 5 Measured nonlinear pitch damping characteristics at $M=0.92$.[6]

$\alpha \approx -2$ deg in Ref. 1. Until the inlet-like flow condition has been studied as extensively as the dynamic stall condition at $M \leq 0.7$,[1-4] dynamic measurement of the time lag $(\Delta\tau)_{CH}$ and the damping levels $c_{m\theta_1}$ and $c_{m\theta_2}$ will be needed. Even so, the agreement shown in Figs. 7 and 8 confirms the effect of the channel flow time lag. These results, together with those in Ref. 1, provided the confirmation of the analytic method needed before it could be applied to compute the aeroelastic characteristics of the Space Shuttle cable trays.[9,10]

Plunging Motion

For the channel flow effect on the plunging cross section, one needs only to compute c_{nz}, since $c_{n\dot{z}} = -C_{n_z}(\Delta\tau)_{CH}$. c_{nz} can be computed by adding the effect of the plunging degree of freedom (z) to the expression for Cp in Eq. (6).

$$C_p = 1-(1-C_{p_b})\left[\frac{(\Delta h - z)c-(\alpha/2)}{(\Delta h - z)c-(\xi-\tfrac{1}{2})\alpha}\right]^2 \tag{13}$$

Differentiating Eq. (13) produces the following derivative

$$\frac{\partial C_p}{\partial(z/c)} = (1-C_{p_b})\frac{2(1-\xi)\alpha[(\Delta h - z)/c-(\alpha/2)]}{[(\Delta h - z)/c-(\xi-\tfrac{1}{2})\alpha]^3} \tag{14}$$

As $\alpha/[(\Delta h - z/c)] << 1$, Eq. (14) can be simplified to

$$\frac{\partial C_p}{\partial\left(\frac{z}{c}\right)} \approx (1-C_{p_b})\frac{2\alpha}{\left(\frac{\Delta h - z}{c}\right)^2}(1-\xi) \tag{15}$$

Thus, the incompressible derivative c_{nz} is obtained as

$$c_{nz} = \frac{\partial c_n}{\partial\left(\frac{z}{c}\right)} = -\int_0^1 \frac{\partial C_p}{\partial\left(\frac{z}{c}\right)}\,d\xi = -\frac{(1-C_{p_b})\alpha}{\left(\frac{\Delta h - z}{c}\right)^2} \tag{16}$$

That is, the translatory derivative c_{nz} at $z=0$ [Eq. (16)] is related to the α derivative at $\alpha=0$ [Eq. (8)] as follows

$$c_{nz} = -(c_{n\alpha})_{CH}\alpha/(\Delta h/c) \tag{17}$$

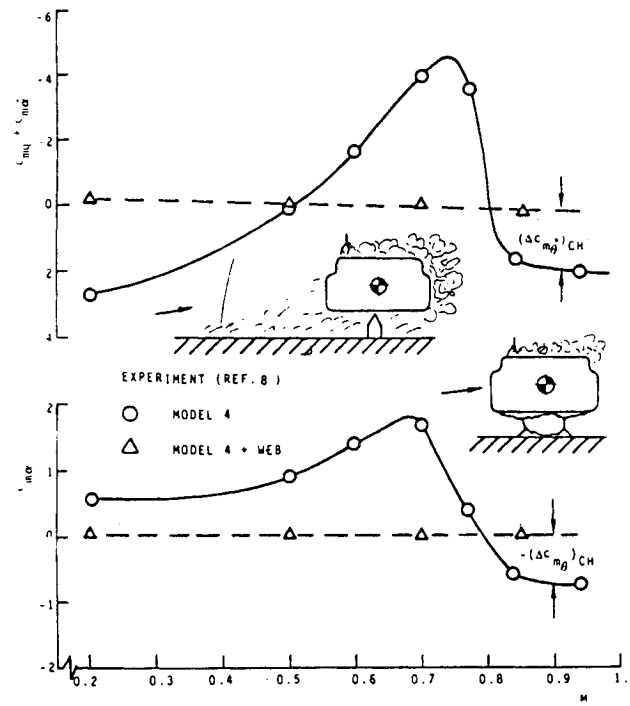

Fig. 6 Effect of flow restriction web on measured damping at $\alpha=0$.[8]

The infinitesimal amplitude plunging derivative on both sides of the discontinuity is given by

$$c_{n\dot{z}} = -c_{nz}(\Delta\tau)_{CH} \tag{18}$$

The time lag $(\Delta\tau)_{CH}$ is the same as for the moment characteristics discussed earlier.

The effect of the plunging degree of freedom on the discontinuous aerodynamic characteristics s ill be evaluated next.

When the critical deflection $z=z_d$ has been exceeded, it takes a final time Δt before the discontinuous force change Δc_n is realized. For harmonic oscillations, $z=\Delta z \sin\omega t$, one obtains

$$z = \Delta z \sin(\psi-\beta) \tag{19}$$

where $\psi=\omega t$ and $\beta=\omega\Delta t=\bar{\omega}\Delta\tau$.

Equation (19) is illustrated graphically in Fig. 9b.

In Fig. 9a the critical value is graphed at $z_d>0$. It can be at any location within the striking range of the oscillation, $-z \leq z_d \leq z$. z_d is determined by the angle of attack at which the plunging oscillation is performed. Allowing for aerodynamic hysteresis, $\Delta z_h \neq 0$, the normal force variation with z is as follows (see Fig. 9a).

$$c_n = \begin{cases} c_{n\dot{z}_1}\dfrac{\dot{z}}{V} & \text{for } \begin{cases} z \leq z_d - \Delta z_h \\ z < z_d;\ \dot{z}>0 \end{cases} \\ c_{n\dot{z}_2}\dfrac{\dot{z}}{V} + \Delta c_n & \text{for } \begin{cases} z \geq z_d \\ z > z - \Delta z_h;\quad \dot{z}<0 \end{cases} \end{cases} \tag{20}$$

where $\bar{c}_{n\dot{z}} = c_{n\theta} + c_{n\dot{z}}$.

The nonlinear damping analysis of Ref. 1 will be modified to apply to the present case of translatory oscillation. In the nonlinear case, one can define a linear measure $c_{\hat{n}\dot{z}}$ of the energy dissipation per oscillation cycle, which becomes $c_{n\dot{z}}$

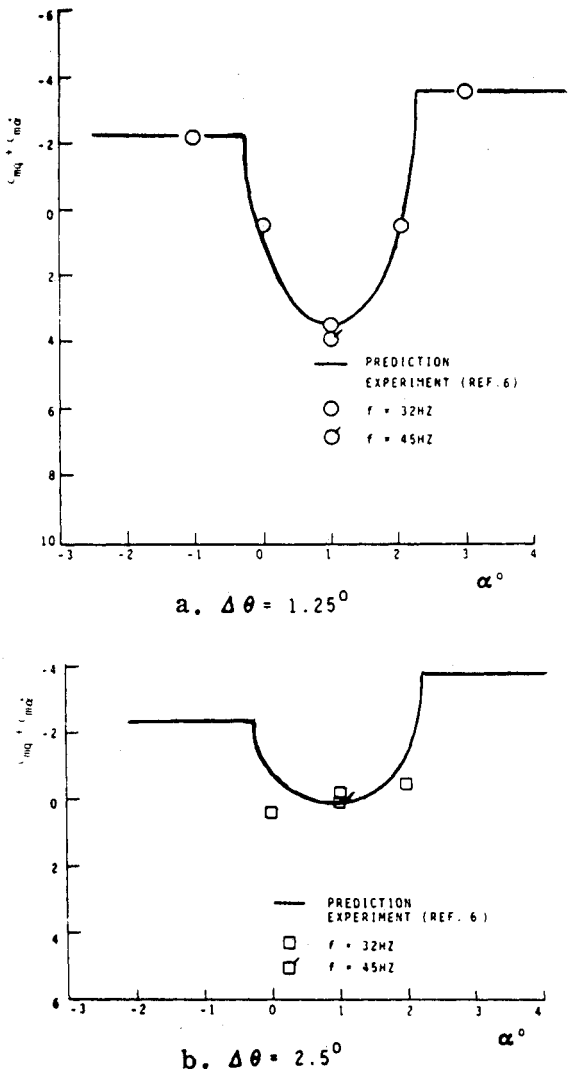

Fig. 7 Comparison between measured and predicted nonlinear pitch damping characteristics at $M=0.92$.

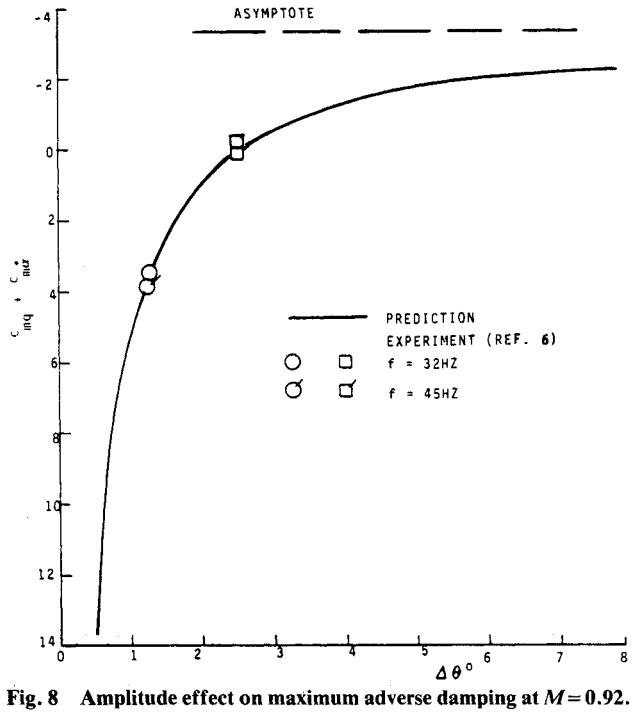

Fig. 8 Amplitude effect on maximum adverse damping at $M=0.92$.

when the nonlinearity disappears. For oscillations $z=\Delta z \sin \omega t$, where $\Delta z = c\Delta\zeta$ and $c\omega/V=\bar{\omega}$, one obtains the following expressions for the energy dissipation per cycle

$$\int c_n \mathrm{d}z = -c_{\dot{n}_{\dot{z}}} \int \frac{\dot{z}}{V}\mathrm{d}z \tag{21}$$

That is,

$$-c_{\dot{n}_{\dot{z}}} = \int_{t_0}^{t_0+2\pi/\omega} c_n \dot{z}\mathrm{d}t \Big/ \int_{t_0}^{t_0+2\pi/\omega} \frac{\dot{z}}{V}\dot{z}\mathrm{d}t = \int_{\psi_0}^{\psi_0+2\pi} c_n \cos\psi \mathrm{d}\psi \Big/ \pi\bar{\omega}\Delta\zeta \tag{22}$$

or

$$-c_{\dot{n}_{\dot{z}}} = \frac{1}{\pi\bar{\omega}\Delta\zeta}\int_{\psi_0}^{\psi_0+2\pi} c_n \cos\psi \mathrm{d}\psi \tag{23}$$

With c_n defined by Eq. (20), Eq. (23) gives the effective dynamic derivative $c_{\dot{n}_{\dot{z}}}$ in the following form for oscillation amplitudes large enough to include the hysteresis loop (see Fig. 9b). (Note that $\dot{z}/V=\Delta\zeta\bar{\omega}\cos\psi$, where $\Delta\zeta=\Delta z/c$.)

$$c_{\dot{n}\dot{z}} = \frac{1}{\pi}\int_{\beta'+\psi_1}^{\beta'+\pi-\psi_2}\left(\bar{c}_{n\dot{z}_2}\cos^2\psi + \frac{\Delta c_n}{\bar{\omega}\Delta\zeta}\cos\psi\right)\mathrm{d}\psi + \frac{1}{\pi}\int_{\beta'+\pi-\psi_2}^{\beta'+2\pi-\psi_1}\bar{c}_{n\dot{z}_1}\cos^2\psi\,\mathrm{d}\psi \tag{24}$$

where

$$\psi_1 = \arcsin\left(\frac{z_d}{\Delta z}\right),\quad \psi_2 = \arcsin\left(\frac{z_d-\Delta z_h}{\Delta z}\right)$$

The integration gives

$$c_{\dot{n}\dot{z}} = \tfrac{1}{2}(\bar{c}_{n\dot{z}_1}+\bar{c}_{n\dot{z}_2}) + (\bar{c}_{n\dot{z}_1}-\bar{c}_{n\dot{z}_2}) \times\left\{\frac{\psi_1+\psi_2}{\pi}+\frac{1}{4\pi}[\sin 2(\beta+\psi_1)-\sin 2(\beta-\psi_2)]\right\} - \frac{\Delta c_n}{\pi\bar{\omega}\Delta\zeta}[\sin(\beta+\psi_1)+\sin(\beta-\psi_2)] \tag{25}$$

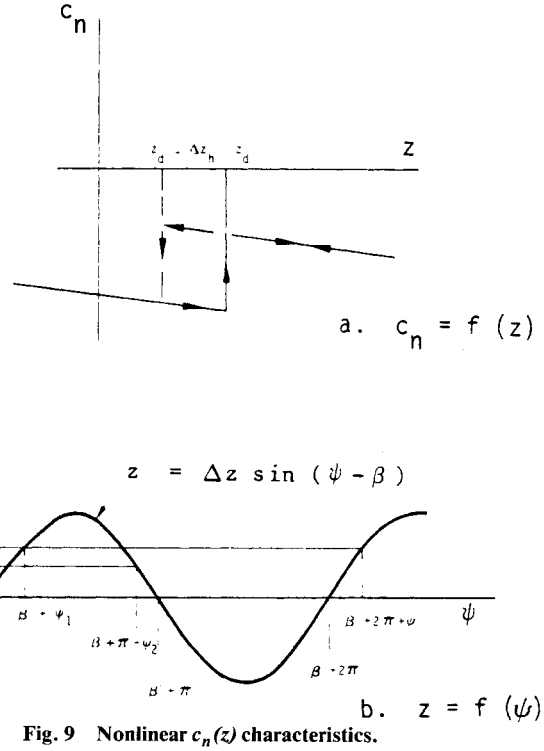

Fig. 9 Nonlinear $c_n(z)$ characteristics.

The dynamic test results[6] showed that there were no hysteresis effects. Thus, $\Delta z_h = 0$ and Eq. (25) becomes

$$c_{\dot{n}\dot{z}} = \frac{\bar{c}_{n\dot{z}_1} + \bar{c}_{n\dot{z}_2}}{2} + \frac{\bar{c}_{n\dot{z}_1} - \bar{c}_{n\dot{z}_2}}{\pi} \arcsin\left(\frac{z_d}{\Delta z}\right) + \left(\frac{z_d}{\Delta z}\right)\sqrt{1-\left(\frac{z_d}{\Delta z}\right)^2}\cos(2\bar{\omega}\Delta\tau) - \frac{2\Delta c_n}{\pi\bar{\omega}\Delta\zeta}\sin(\bar{\omega}\Delta\tau)\sqrt{1-\left(\frac{z_d}{\Delta z}\right)^2} \tag{26}$$

For the low frequencies in the dynamic test[6], $\bar{\omega}^2 << 1$, Eq. (26) can be simplified further to the following form.

$$c_{\dot{n}\dot{z}} = \frac{\bar{c}_{n\dot{z}_1} + \bar{c}_{n\dot{z}_2}}{2} + \frac{\bar{c}_{n\dot{z}_1} - \bar{c}_{n\dot{z}_2}}{\pi} \times \left[\arcsin\left(\frac{z_d}{\Delta z}\right) + \left(\frac{z_d}{\Delta z}\right)\sqrt{1-\left(\frac{z_d}{\Delta z}\right)^2}\right] - \frac{2\Delta c_n \Delta\tau}{\pi\Delta\zeta}\sqrt{1-\left(\frac{z_d}{\Delta z}\right)^2} \tag{27}$$

In regard to the dynamic test,[6] the results in Fig. 5 indicate that the plunging test was performed at or very close to $\alpha = \alpha_d$ where $z_d = 0$ (zero.) (At $\alpha = \alpha_d$ an infinitesimal perturbation, $\Delta z \to 0$, will "catch" the discontinuity.) This also gives the maximum effect of the discontinuous aerodynamics.

Setting $z_d = 0$ in Eq. (27) gives

$$c_{\dot{n}\dot{z}} = \frac{\bar{c}_{n\dot{z}_1} + \bar{c}_{n\dot{z}_2}}{2} + \frac{2\Delta c_n \Delta\tau}{\pi\Delta\zeta} \tag{28}$$

As the topside flow is completely separated, wakelike in character, it contributes nothing to the infinitesimal amplitude damping on both sides of the discontinuity. The channel flow contribution is obtained from Eqs. (8), (17) and (18), as was discussed earlier. For the ground interference effect at $M = 0.7$ and $\alpha = -2$ deg, the time lag $(\Delta\tau)_{CH}$ can be computed as described in Ref. 1.

At $M = 0.7$ and $\alpha < -2$ deg, where the regular ground plane interference exists, the complete derivative $\bar{c}_{n\dot{z}}$ is

$$\bar{c}_{n\dot{z}} \approx c_{n\theta}/2 + c_{n\dot{z}} \tag{29}$$

At $M = 0.9$ and $\alpha > 0$, where the channel flow is choked, one obtains

$$\bar{c}_{n\dot{z}} = c_{n\dot{z}} = 2.18 \tag{30}$$

Going to Fig. 2a to obtain Δc_n, one finds that no c_n-jump†† is occurring at $M = 0.7$ between $\alpha = -3$ and -4 deg. The pressure distribution results in Fig. 1a show that at $M = 0.7$ there is not only a contribution $\Delta c_n \approx -0.12$ from the bottom side, but that there is also an opposing c_n-jump, caused by the change of pressure level on the topside. Evidently, when complete flow separation occurs on the bottom side, the resulting decrease in channel mass flow rate causes an increase in the upwash angle, changing the "base pressure" level on the topside (Fig. 10). Thus, the topside contributes $\Delta c_n \approx 0.12$, and the complete characteristics, defined by Eq. (28), are as follows.

Topside:

$$(\Delta c_{n\dot{z}})_{\text{top}} = \frac{2}{\pi}\frac{0.12\Delta\tau}{\Delta\zeta} \tag{31a}$$

Bottomside:

$$(\Delta c_{n\dot{z}})_{\text{bottom}} = -5.95 - \frac{2}{\pi}\frac{0.12\Delta\tau}{\Delta\zeta} \tag{31b}$$

For the topside the pressure change is transmitted almost instantaneously and its contribution to $c_{\dot{n}\dot{z}}$ can be neglected. For the bottomside the analysis in Ref. 1 gave $(\Delta\tau)_{\text{bottom}} = 4.00$. Thus, Eq. (31b) gives

$$c_{\dot{n}\dot{z}} = -5.95 - \frac{0.335}{\Delta\zeta} = -5.95 - 0.67\Big/\frac{\Delta z}{h} \tag{32}$$

Figure 11a shows that the experimental data point[6] is in good agreement with the prediction by Eq. (32).

It is obvious that at $M = 0.7$ and $\alpha < -2$ deg, where the channel flow is not choked, it is the presence of the ground plane that permits the flow to reattach at $\alpha \geq -3$ deg, and one can, therefore, expect that closing the gap, $z > 0$, would help to cause sudden reattachment on the bottomside, generating a negative normal force jump, $\Delta c_n < 0$ (Fig. 1a). It is less obvious for the choked channel flow, existing at $M = 0.9$ and $\alpha > 0$, what the effect will be of closing the gap, $z > 0$. It not only has the effect of restricting the channel exit area, as for increasing α, but it also increases the channel inlet velocity. This is similar to what is obtained through an increase of M, from $M = 0.9$ to 1.05, for example. Figure 2 shows that the M effect counteracts the α effect, moving the discontinuity from $\alpha_d \approx 1$ deg at $M = 0.9$ to $\alpha_d \approx 2$ deg at $M = 1.05$. Thus, closing the gap, $z > 0$, will cause a positive normal force jump, $\Delta c_n > 0$, if the α effect dominates, but a negative force jump, $\Delta c_n < 0$, if the M effect dominates. More extensive static experimental results, for z variations in addition to α variations, would have resolved this dilemma. In the present case, however, one has to use both assumptions and see which one is in agreement with the dynamic data trend.

At $M = 0.9$, Fig. 2a gives $|\Delta c_n| \approx 0.15$. Thus, according to the preceding discussion, Eqs. (28) and (30) give

$$c_{\dot{n}\dot{z}} = 2.18 \pm \frac{2|\Delta c_n|\Delta\tau_{CH}}{\pi\Delta\zeta} \tag{33}$$

With $\Delta\tau_{CH} = 2.8$, as before, one obtains

$$c_{\dot{n}\dot{z}} = 2.18 \pm 0.535\Big/\frac{\Delta z}{h} \tag{34}$$

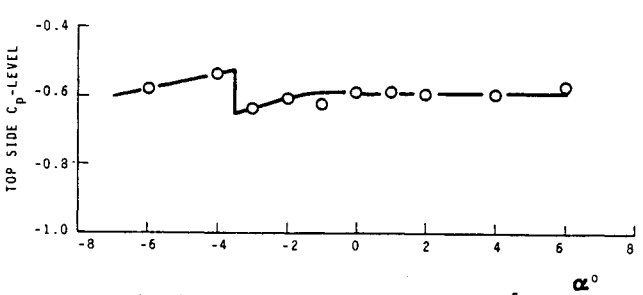

Fig. 10 Topside pressure level at $M = 0.7$.[5]

††The c_n-jump occurring between $\alpha = -2$ and -3 deg was not captured in the dynamic test.[6]

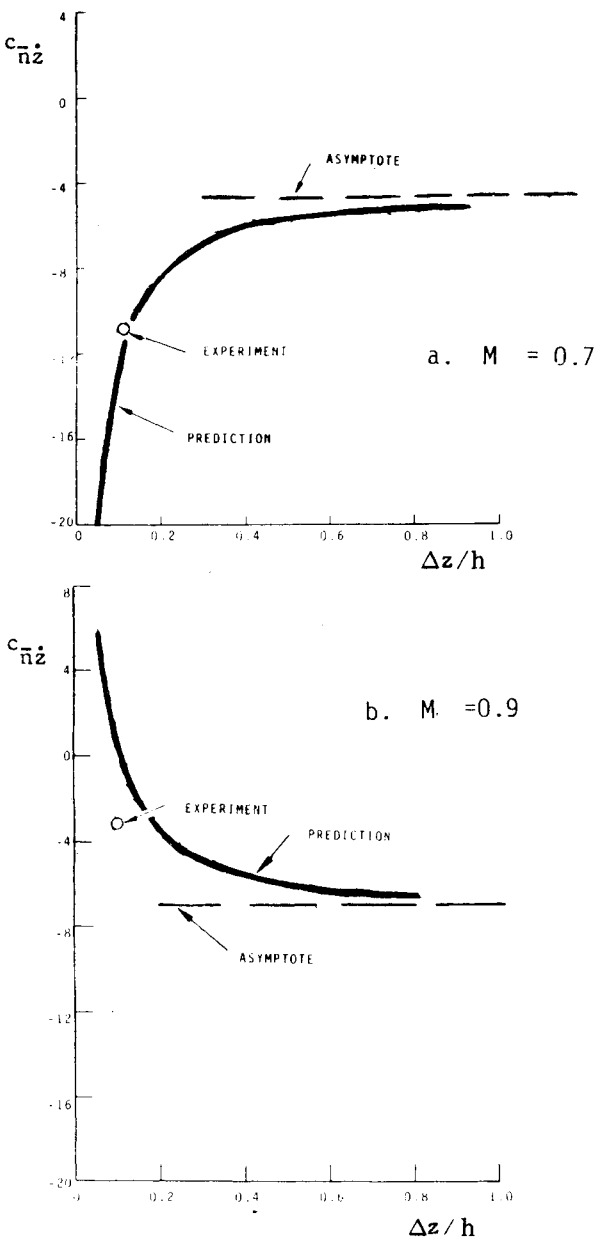

Fig. 11 Nonlinear damping characteristics for translatory oscillations.

When comparing the results of Eq. (34) with the experimental data point[6] (Fig. 11b), it becomes clear that the M effect dominates and only the minus sign in Eq. (34) applies. This is also in agreement with additional results in Ref. 6 for the same cross section, which show the ground plane to have a dynamically stabilizing influence on the plunging oscillations.

Conclusions

The developed analytic relationships between unsteady and steady aerodynamic characteristics provide the capability to predict the nonlinear damping characteristics of cross sections describing pitching or plunging oscillations close to a ground plane. For unchoked flow conditions in the channel between airfoil and ground plane the only requirement is that the static aerodynamic characteristics are known (e.g., through detailed static wind tunnel tests). For choked flow conditions, additional, selected dynamic measurements are presently needed to establish the flowfield time lag. The veracity of the method has been demonstrated by successful prediction of the highly nonlinear dynamic experimental results for a rectangular, indented cross section, representing one design of the Space Shuttle cable trays for which large ground interference effects are present at transonic cross-flow conditions.

References

[1]Ericsson, L. E. and Reding, J. P., "Shock-Induced Dynamic Stall," *Journal of Aircraft*, Vol. 21, May 1984, pp. 316-321.

[2]Ericsson, L. E. and Reding, J. P., "Dynamic Stall Analysis in Light of Recent Numerical and Experimental Results," *Journal of Aircraft*, Vol. 13, April 1976, pp. 248-255.

[3]Ericsson, L. E. and Reding, J. P., "Dynamic Stall at High Frequency and Large Amplitude," *Journal of Aircraft*, Vol. 17, March 1980, pp. 136-142.

[4]Reding, J. P. and Ericsson, L. E., "Analysis of Static and Dynamic Wind Tunnel Tests of the Space Shuttle Cable Trays," *Journal of Spacecraft and Rockets*, Vol. 19, No. 5, Sept-Oct. 1982, pp. 412-418.

[5]Michna, P. J. and Parker, D. R., "Test Results from the Pressure Test of a .12 Scale Model of the External Tank LO Cable Tray and GO Pressure Line and a .1575 Scale Model of the Aft ET/SRB Cable Tray in the MSFC 14 Inch Trisonic Wind Tunnel Test No. TWT 661," Rept. MMC-ET-SE05-89, Martin-Marietta Corp., Michoud Operations, New Orleans, La., May 1980.

[6]Orlik-Rückemann, K. J. and LaBerge, J. G., "Dynamic Wind Tunnel Tests of the Simulated Shuttle External Tank Cable Trays," *Journal of SPacecraft and Rockets*, Vol. 20, Jan.-Feb. 1983, pp. 5-10.

[7]Borst, H. V., "Analysis of Vehicles With Wings Operating in Ground Effect," AIAA Paper 79-2034, Oct. 1979.

[8]LaBerge, J. G., "Dynamic Wind Tunnel Tests if the Shuttle External Tank Cable Trays at Subsonic Speeds," LTR-UA+55, NRC, Canada, Feb. 1981.

[9]Ericsson, L. E and Reding, J. P., "Aeroelastic Analysis of the Space Shuttle External Tank Cable Trays," Final Tech. Rept. LMSC D766543, Lockheed Missiles & Space Company, Inc., Sunnyvale, Calif., April 1981.

[10]Ericsson, L. E. and Reding, J. P., "Aeroelastic Characteristics of the Space Shuttle External Tank Cable Trays," AIAA Paper 82-0633, May 1982.